京都大学学術情報リポジトリ

KURENAI 紅

Kyoto University Research Information Repository

Paper:

# Estimating the Volcanic Ash Fall Rate from the Mount Sinabung Eruption on February 19, 2018 Using Weather Radar

**Magfira Syarifuddin**[*1,†], **Satoru Oishi**[*2], **Ratih Indri Hapsari**[*3], **Jiro Shiokawa**[*4],
**Hanggar Ganara Mawandha**[*4], **and Masato Iguchi**[*1]

[*1]Sakurajima Volcano Research Center, Disaster Prevention Research Institute (DPRI), Kyoto University
1722-19 Sakurajima-Yokoyama, Kagoshima 891-1419, Japan
[†]Corresponding Author, E-mail: syarifuddin.magfira.8a@kyoto-u.ac.jp
[*2]Research Centre for Urban Safety and Security, Kobe University, Hyogo, Japan
[*3]Department of Civil Engineering, State Polytechnic of Malang, Malang, Indonesia
[*4]Graduate School of Engineering, Kobe University, Hyogo, Japan

This paper presents a theoretical method for estimating volcanic ash fall rate from the eruption of Sinabung Volcano on February 19, 2018 using an X-band multi-parameter radar (X-MP radar). The X-MP radar was run in a sectoral range height indicator (SRHI) scan mode for 6° angular range (azimuth of 221°–226°) and at an elevation angle of 7° to 40° angular range. The distance of the radar is approximately 8 km in the Southeastern direction of the vent of Mount Sinabung. Based on a three-dimensional (3-D) image of the radar reflectivity factor, the ash column height was established to be more than 7.7 km, and in-depth information on detectable tephra could be obtained. This paper aims to present the microphysical parameters of volcanic ash measured by X-MP radar, which are the tephra concentration and the fall-out rate. These parameters were calculated in a two-step stepwise approach microphysical model using the scaled gamma distribution. The first step was ash classification based on a set of training data on synthetic ash and its estimated reflectivity factor. Using a naïve Bayesian classification, the measured reflectivity factors from the eruption were classified into the classification model. The second step was estimating the volcanic ash concentration and the fall-out rate by power-law function. The model estimated a maximum of approximately 12.9 g·m$^{-3}$ of ash concentration from the coarse ash class (mean diameter $D_n = 0.1$ mm) and a minimum of approximately 0.8 megatons of volcanic ash mass accumulation from the eruption.

**Keywords:** volcanic ash, X-MP radar, ash microphysical model, radar remote sensing, volcanic eruption

## 1. Introduction

Mount Sinabung (3.17°N, 98.39°E) in Karo Regency, North Sumatera Province of Indonesia (**Fig. 1**) is a stratovolcano with an elevation of 2460 m above sea level (asl). This single peak volcano has been active since 2010, after a dormant period of more than 400 years [1]. One of its latest eruptions on February 19, 2018, at 08:53 local time, lasted for 291 s and released volcanic plume to a height of approximately 7460 m. This eruption caused some cancelation of flights to and from Kualanamu Airport in Medan. The ash rain reached Aceh Province at the northern end of Sumatera (more than 250 km from the summit of Mt. Sinabung) [2].

Materials of all types and sizes that erupt from a crater or volcanic vent as a result of an intensive magma and rock fragmentation are usually referred to as tephra. Tephra or volcanic ash is one of the major hazards to life and property. Small quantities of ash can cause inconveniences such as water pollution and the disruption of agriculture and transportation.

The monitoring of volcanic ash involves methods such as photography, field sampling, and ground tephra deposit analysis. However, these methods have some known limitations and disadvantages. Field sampling and tephra deposit analysis can provide only indirect information about the microphysical characteristics because several processes can take place during the ejection and the fall-out [3].

The photographic method provides real-time information, but it provides only two-dimensional (2-D) images of the eruption scene. Furthermore, the minimum size of particle ash that can be resolved is usually limited. This method relies on the infrared wavelength: hence it has better performance during night observation, causing non-continuous observation [4]. By dealing with these limitations, remote sensing techniques from both ground and space represent unique tools to be exploited [4, 5].

Recently, there has been much interest in the use of weather radar in volcanic ash retrieval. The weather radar
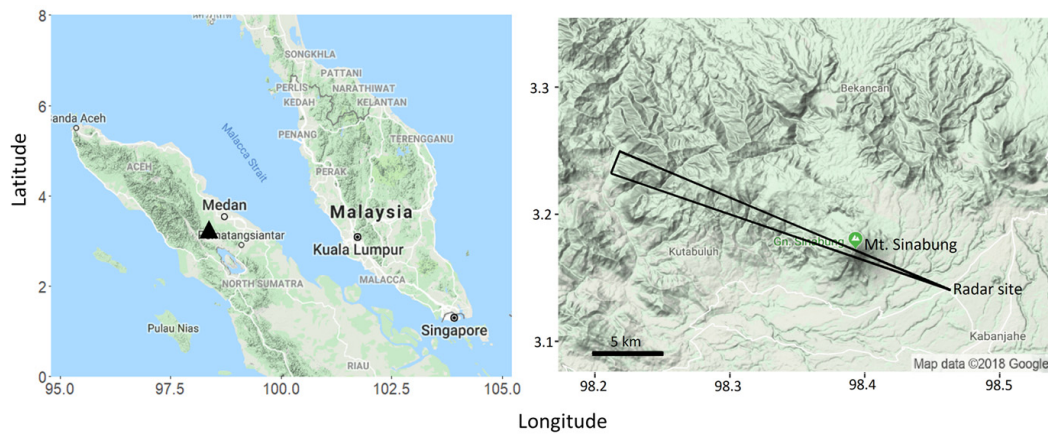
京都大学
KYOTO UNIVERSITY

Syarifuddin, M. et al.

京都大学学術情報リポジトリ
KURENAI 紅
Kyoto University Research Information Repository

**Fig. 1.** The location of Mt. Sinabung in Sumatra Island of Indonesia (left) indicated by the black triangle, and the zoom area monitor by SRHI scan mode at Mt. Sinabung, delineated by black line (right).

presents three-dimensional (3-D) information on atmospheric scattering volume over a relatively wide region despite weather conditions. The data is also presented in fine spatial resolution (several meters to less than a kilometer, depending on the radar wavelength), within a few minutes to seconds temporal resolution [6–11].

The ground-based radar system represents one of the best methods for determining the height and volume of volcanic eruption clouds. Studies on volcanic ash retrieval by radar have been conducted since 1983 [8]. However, the numbers are not yet as well established as those on rainfall retrieval by radar. In 1998, the first deployment of Volcanic Doppler Radar (VOLDORAD) successfully monitored the eruption of Mt. Etna in Italy [12]. The VOLDORAD revealed powerful echoes during the eruption paroxysm (lava fountains), which gradually decreased along with declining activity. Nevertheless, this radar runs at L-frequency (1.5 GHz), which provides it a coarser resolution and may not be suited to the fine size of volcanic ash. It also operates at medium range (until 5.5 km), which limits its practical application for remote sensing purposes [12].

Using a polarimetry radar, Marzano et al. have conducted some comprehensive studies in remote sensing for volcanic ash monitoring [3, 10, 11]. The studies used four types of weather radar systems: S-band, C-band, X-band, and Ka-Band to monitor the volcanic ash cloud. They revealed that the sensitivity of radar to monitoring the ash cloud was reliable until X-band, while the shorter wavelength of the Ka-band system was greatly attenuated. The path attenuation of Ka-band radar could reach several decibels per km, which was high compared to a maximum of 0.15 dB/km for C and S-band radar, and a maximum of 1 dB/km for X-band [10]. Another study had a similar result, in which a higher ground radar frequency of 94 GHz gave a strong attenuation to volcanic ash observation [13].

Further development and studies in weather radar have proven the ability of multiparameter radar to provide better rainfall information [14]. However, its application to

quantitative volcanic ash estimation is still unexplored. A qualitative analysis of volcanic ash was done in Sakurajima, Japan using two X-band multi-parameter (X-MP) radars. However, the study was limited to the detection of volcanic ash and to proving the ability of X-MP radar to monitor the weak echo caused by the ejected volcanic ash and its movement. The study did not provide quantitative information on the volcanic ash parameters estimated by the radar [15].

The eruption of Mt. Sinabung in Indonesia on February 19, 2018, was monitored by an X-MP radar located 8 km southeast from the vent (**Fig. 1**). This radar is compact, small, and able to acquire the data for 100 m mesh resolution every 50 s. This specification allows the radar to gain detailed information on the vertical profile inside the volcano ash cloud, and on the movement of particle ash inside the cloud, within seconds. This information is still limited because (1) a previous similar study used S-band and C-band radar, which gave coarser time and spatial resolution of the ash cloud vertical profile, (2) the previous X-band radars used are located far from the volcano, which reduced the signal strength [3].

The objective of this study is to estimate the microphysical parameters of volcanic ash, which are ash concentration and fall-out rate. Though the study is not supported by a field verification, it enhances the ideas on the remote sensing technique of volcanic ash monitoring by weather radar. This kind of study is an important aspect of the scientific and technological advances in radar and volcanology.

## 2. Radar Data Acquisition

The installed X-MP radar on Mt. Sinabung is a FURUNO WR 2100, with 3.3 cm wavelength and 9.47 GHz frequency. **Table 1** provides the specifications and the multi-parameters measured by the X-MP radar. The radar is set at an altitude of 1057 m, at coordinates 3.14°N and

**Table 1.** Specifications of the X-MP radar installed near Mt. Sinabung.

| Parameter | Description |
|---|---|
| Transmitter | Solid state 200 W per channel (H,V) |
| Polarity | Dual polarimetric horizontal (H) and vertical (V) |
| Pulses | PRF 600–2500 Hz, Width 0.1–5.0 $\mu$s |
| Antenna | 0.75 m $\emptyset$, 2.7° beam width |
| Antenna gain | 33.0 dBi |
| Operating Frequency | 9.47 GHz |
| Wavelength | 3.3 cm |
| Scan mode | PPI, CAPPI, RHI |
| Maximum distance display | 50 km |
| Maximum range fixed observation level | 30 km |
| Data Output | Reflectivity Intensity: $Z_H$ (dBZ), Differential reflectivity: $Z_{dr}$ (dB), Doppler velocity: $V_D$ (m·s$^{-1}$), Doppler velocity spectrum width: $\sigma_{VD}$ (m·s$^{-1}$) Specific differential phase shift: $K_{DP}$ (°km) Copolar correlation coefficient: $\rho_{HV}$ Rainfall intensity: $R$ (mm·h$^{-1}$), Cross polarization difference phase: $\Phi_{DP}$ |

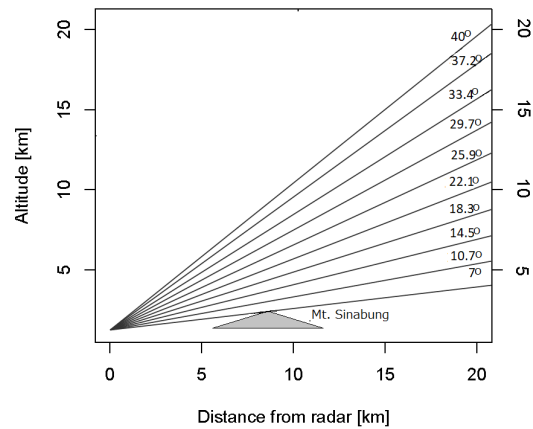Source: Furuno, WR 2100 operator manual handbook



**Fig. 2.** Altitude range and distance from radar for the SRHI scan mode set by X-MP radar.

98.46°E. During the eruption, the radar scan mode was set to sector range height indicator (SRHI), at the azimuth angular range between 221°and 226°. The elevation angle was set at the range of 7°to 40°.

**Figures 1** and **2** give the location of Mt. Sinabung, the area monitored by SRHI scan mode, and the elevation range, respectively. The scan mode has limited the maximum altitude which could be monitored by the X-MP radar to 7.7 km above the peak of Mt. Sinabung (approximately 10 km asl).

## 3. Volcanic Ash Retrieval by Weather Radar

Volcanic ash has some important characteristics that distinguish it from rainfall: (1) Ash quantity and size distributions can be preserved in the atmosphere or on the ground near the volcano vent for very long periods. (2) The ash particle size distribution (PSD) is mainly established by explosive fragmentation rather than by reversible processes such as condensation, evaporation, coalescence, and breakup. In contrast with rain clouds, in situ sampling of ash clouds by aircraft is not possible, except during very light ash fall, because ash clouds can be a major hazard to aircraft flight. In this research, we adopted the volcanic ash retrieval by radar (VARR) model developed by Marzano et al. [10, 11], which fol-

lows the same theoretical approach as rainfall retrieval models based on scaled gamma distribution. There are several reasons to adopt this method:

- As the SRHI scan data did not cover the entire volume of volcanic ash, we decided to focus on the insight aspect of volcanic ash clouds.

- There was no ground verification to measure the ground PSD, and the ground volcanic ash nature may be different from ash nature during the eruption.

- The empirical model of volcanic ash fall rate and the multi-parameters of radar have not been significantly well developed, which makes it necessary to adopt the basic radar equation for rain in the ash retrieval model.

### 3.1. Microphysical Model of Volcanic Ash Radar Reflectivity

The following subsections explain the quantitative definitions and methods for the physical parameterization of the volcanic ash cloud, the assumptions, and the limitations the model, which is based on the VARR model of Marzano et al. [10, 11].

#### 3.1.1. Volcanic Ash Parameterization

The PSD describes the particle occurrence per unit volume and unit size. It expresses as per centimeter to the fourth power (cm$^{-4}$) or per cubic meter per millimeter (m$^{-3}$·mm$^{-1}$). PSD plays a significant role in determining the backscattering and absorption properties of a particle ensemble [10]. The ash PSD is indicated by $N_a(D)$, where $D$ [mm] is the particle diameter. The gamma PSD as a general scaled form of $N_a(D)$ [m$^{-3}$·mm$^{-1}$] is formally expressed as:

$$N_a(D) = N_n \left( \frac{D}{D_n} \right)^{\mu} e^{-\Lambda_n \left( \frac{D}{D_n} \right)^{\upsilon}} \quad \ldots \ldots \quad (1)$$

京都大学
KYOTO UNIVERSITY

A Self-archived copy in
Kyoto University Research Information Repository
https://repository.kulib.kyoto-u.ac.jp

KURENAI 紅
Kyoto University Research Information Repository

Syarifuddin, M. et al.

where $D_n$ [mm] is the number-weighted mean diameter; in a logarithmic plane, $N_n$ [m$^{-3}$·mm$^{-1}$] is the intercept; $\Lambda_n$ is the slope; $\mu$ is the shape factor; $\upsilon$ is the slope factor. The normalization is such that $N_n$ and $\Lambda_n$ are related to the mean diameter $D_n$ and ash concentration $C_a$, and have physical dimensions independent of $\mu$ and $\upsilon$.

A simple unimodal form [10] is adopted as it provides a more consolidated assumption of the average size distribution. The PSD form follows the scaled gamma PSD, which is derived from the analogs form established for raindrops. The scaled gamma PSD $N_{SG}$ assumes that $\upsilon = 1$, and follows an equation similar to Eq. (1):

$$N_{SG}(D; \mu, D_n, C_a) = N_{nG}\left(\frac{D}{D_n}\right)^{\mu} e^{-\Lambda_{nG}\left(\frac{D}{D_n}\right)}, \quad . \quad (2)$$

where the intercept parameter $N_{nG}$ and the slope parameter $\Lambda_{nG}$ were scaled using this equation:

$$\begin{cases} N_{nG} = C_a \dfrac{6D_n^{\mu}}{\pi \rho_a (3+\mu)!} \left[\dfrac{(\mu+1)!}{D_n(\mu!)}\right]^{3+\mu+1} \\ \Lambda_{nG} = \mu + 1 \end{cases} \quad . \quad (3)$$

The $N_{SG}$ in this model has the following properties [10]:

- It is specified by three parameters, $\mu$, $D_n$, and $C_a$, using Eq. (3), and assuming an ash constant density $\rho_a$ and spherical (or equivalent spherical) particles.

- $N_{nG}$ has a dimension which is $\mu$-independent and given in [mm$^{-1}$·m$^{-3}$].

- $\Lambda_{nG}$ is dimensionless.

Mass concentration $C_a$ [g·m$^{-3}$] of sphere equivalent particles is given by

$$C_a = \frac{\pi}{6}\rho_a m_3 \quad . \quad . \quad . \quad . \quad . \quad . \quad . \quad . \quad . \quad . \quad . \quad (4)$$

The ash fall rate $R_a$ [kg·h$^{-1}$·m$^{-2}$], which is defined as the particle mass crossing the horizontal cross section of a unit area over a given interval of time, can be expressed by the following formula [11]:

$$R_a = 3.6 \times 10^{-3}\left[\frac{\pi}{6}a_v\rho_a m_3 + b_v\right], \quad . \quad . \quad . \quad . \quad (5)$$

where $\rho_a$ is the mass density of volcanic ash, $m_3$ is the third moment of gamma distribution, $a_v$ [m·s$^{-1}$] and $b_v$ are empirical coefficients that can also take into account the correction for the height-dependent air density. The parameters $a_v$ and $b_v$ are constants given by the analysis of *in situ* data on ash fall terminal velocity as a function of ash diameter from the Mount St. Helens eruption in 1980, which are $a_v = 7.46$ m·s$^{-1}$ and $b_v = 1.0$ [16].

The $n$-th moment of gamma distribution is given by

$$m_n = \int_{D_1}^{D_2} D^n N_a(D)\,dD. \quad . \quad . \quad . \quad . \quad . \quad . \quad (6)$$

Using the assumption of $\mu = 1$, then an explicit expression of the complete moment of gamma distribution (i.e., when $D_1 = 0$ and $D_2 = \infty$) can be written as follows:

$$m_{nG} = \frac{N_{nG}}{(\Lambda_{nG})^{n+2}} D_n^{n+2-\mu} \Gamma(n+2), \quad . \quad . \quad . \quad (7)$$
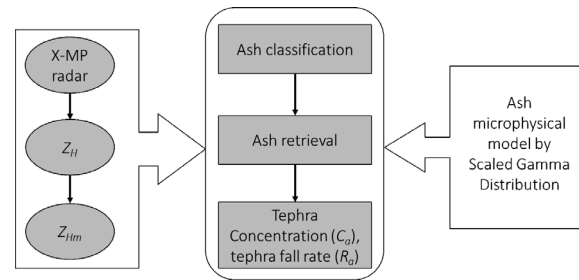


**Fig. 3.** Schematic diagram of the VARR algorithm, trained by the microphysical radar model [11]. $Z_{Hm}$ is the corrected measured reflectivity ($Z_H$), while $C_a$ and $R_a$ are the tephra/ash concentration and fall rate, respectively.

where $\Gamma$ is the gamma function, while $N_{nG}$ and $\Lambda_{nG}$ are derived from Eq. (3).

### 3.1.2. Radar Reflectivity and its Approximation

The model assumes the particles follow Rayleigh scattering approximation, as a previous sensitivity analysis has shown that this approximation is well satisfied for radar ash observations up to X-band [10]. Based on the previous study, the related specific attenuation is negligible as it usually holds values less than 0.1 dB/km even for intense ash concentration at X-band [10, 11]. In the Rayleigh scattering assumption, the polarized radar reflectivity factor (also mentioned as radar reflectivity) $Z_H$ [mm·m$^{-6}$] is given by the sixth moment of gamma distribution:

$$Z_H = \int_{D_{\min}}^{D_{\max}} D^6 N_a(D)\,dD = m_6. \quad . \quad . \quad . \quad . \quad . \quad (8)$$

### 3.2. Procedures of Volcanic Ash Retrieval by Microphysical Model

The general procedure of VARR was developed according to the Marzano et al. model [10, 11], which is summarized in **Fig. 3**. The determination of a scaled gamma particle size distribution (SG-PSD) to cover the microphysical model of volcanic ash for $D_1 = 0$ and $D_2 = \infty$ was implemented by following these steps:

- Determining the ash density $\rho_a$.

- Assigning $D_n$, $C_a$, and $\mu$.

- Computing $\Lambda_{nG}$ and $N_{nG}$ using Eq. (3).

The ash density $\rho_a$ is constant at $10^6$g·m$^{-3}$ and $\mu = 1$ [10, 11, 13], $D_n$ and $C_a$ are based on ash classes from a previous study [10] presented in **Table 2**. Sections 3.2.1 and 3.2.3 further explain the procedure of VARR.

### 3.2.1. Correction of Radar Reflectivity

The relationship between radar reflectivity ($Z_H$) and the concentration and fall rate follow the power-law equation. The measured reflectivity factor can be obtained

**Table 2.** Classes of average ash size and concentration in terms of average mean values of diameter deviation-mean proportionality [10].

| Mean diameter $D_n$ [mm] | Average mean Diameter $<D_n>$ | Proportionality $\sigma_{Dn}$ and $<D_n>$ |
|---|---|---|
| Fine ash | 0.01 | 20% |
| Coarse ash | 0.1 | 20% |
| Lapili | 1 | 20% |
| Ash concentration $C_a$ [g·m$^{-3}$] | Average concentration $<C_a>$ | Proportionality $\sigma_{Ca}$ and $<C_a>$ |
| Light | 0.1 | 50% |
| Moderate | 1 | 50% |
| Intense | 5.0 | 50% |

from Eq. (8). A zero-mean Gaussian random error $\varepsilon_Z$, with a given standard deviation $\sigma_Z$, is introduced to correct the radar reflectivity factor [11], and is expressed as:

$$Z_{Hm} = Z_H + \varepsilon_Z, \quad . \quad . \quad . \quad . \quad . \quad . \quad . \quad . \quad . \quad . \quad . \quad . \quad (9)$$

where $Z_H$ is measured in decibels referenced to zero (dBZ). An error with a standard deviation $\sigma_Z$ of 1.4 dBZ is used based on the recommendation of the previous study [11] in relation to the systematic bias of radar-measured reflectivity, the attenuation from atmospheric gases and ash particles, partial antenna-beam filling, and ground clutter or anomalous propagation.

### 3.2.2. Ash Classification

The first step of ash classification was to prepare sets of data to determine the characteristics of volcanic ash, which were PSD and $N_{nG}$. Nine sets of synthetic data were generated randomly based on the normal distribution, the criteria of volcanic ash class in **Table 2** [10]. The ash size distribution assessable by weather radar were divided into nine categories classes based on mean values and the proportional deviation of ash particle diameter and concentration.

Calculating the reflectivity factor $Z_{Hm}$ based on Eqs. (8) and (9), nine pairs of $Z_{Hm}$-class set data were obtained. These synthetic reflectivity factor data were used as the training data to generate the probability model of radar reflectivity and the ash classification. This step was done to automatically discriminate between ash categories that were defined based on sizes and those based on concentration regimes.

The classification represents the first qualitative output before performing parameter estimation. It was done by a maximum a posteriori (MAP) probability criterion in a model-based supervised context. This approach was framed within the general naïve Bayesian theorem and offered to insert, in a rigorous manner, both the forward modeling and a priori information.

Using the naïve Bayesian theorem, if $c$ is the ash class, which consists of nine classes presented in **Table 2**, then the conditional probability density function (pdf) of a class $c$, given a measurement $Z_{Hm}(c|Z_{Hm})$, can be expressed as

$$p(c|Z_{Hm}) = \frac{p(Z_{Hm}|c)\,p(c)}{p(Z_{Hm})}, \quad . \quad . \quad . \quad . \quad . \quad . \quad (10)$$

where $p(Z_{Hm}|c)$ is the probability density function of reflectivity belonging to a certain class, and $p(c)$ represents the a priori discrete pdf of a class $c$ [11]. Because there are nine ash classes, the probability density function $p(c)$ is the same at 0.11.

### 3.2.3. Ash Concentration and Fall Rate Estimation

Following the identification of an ash class, an estimation of ash concentration and fall rate is given by a statistical parametric model to describe the relationship $P$–$Z_{Hm}$, where $P$ stands for $C_a$ or $R_a$, by the power-law model assumption [11]. The estimated quantity for each class $c$ of both parameters are as follows:

$$\begin{cases} \hat{C}_a^{(c)} = \alpha[Z_{Hm}]^{\beta} \\ \hat{R}_a^{(c)} = \gamma[Z_{Hm}]^{\delta} \end{cases}, \quad . \quad . \quad . \quad . \quad . \quad . \quad . \quad . \quad . \quad (11)$$

where $c$ is the nine classes of volcanic ash retrieved by radar measurement, the hat ($\wedge$) indicates estimated quantity, while $\alpha$, $\gamma$, $\beta$, and $\delta$ are the constants and the law-exponents.

Compared with the model application by previous studies [10, 11], this study focuses only on X-band system application for the volcanic ash retrieval model; hence the developed algorithms for ash parameters calculation is suitable for only the X-band system.

## 4. Results and Discussion

### 4.1. The Multi-Parameters of X-MP Radar During the Eruption

In the early stage of eruption, the seismic amplitude instrument gave an increase of the Root Mean Square Error (RMSE) of $2.03 \times 10^{-6}$m·s$^{-1}$ at 08:53 local time. The temporal changes of mean values and maximum values of some of the multi-parameters of X-MP radar, which are: reflectivity factor ($Z_H$), differential reflectivity ($Z_{dr}$), specific differential phase shift ($K_{DP}$), and Doppler velocity ($V_D$) are presented in **Figs. 4** and **5**, respectively.

In general, increasing of seismic amplitude is followed by the value change of the multiparameters of radar. The increase of $Z_H$ shows some time-lag differences of approximately 8 min for the next increase in the RMSE seismic amplitude after 02:19 UTC. This $Z_H$ increase could be directly interpreted as the lifespan of volcanic ash existed near the vent.

In **Fig. 4**, the change of differential reflectivity $Z_{dr}$, followed the temporal change of seismic amplitude in almost the same rate. This fact shows the possibility of $Z_{dr}$ to be involved as an estimator of volcanic ash eruption together with $Z_{HH}$, as the $K_{DP}$ cannot give immediate increase after the eruption.

At the 08:53:43 or the similar time of eruption the radar

京都大学
KYOTO UNIVERSITY

Syarifuddin, M. et al.

京都大学学術情報リポジトリ
KURENAI 紅
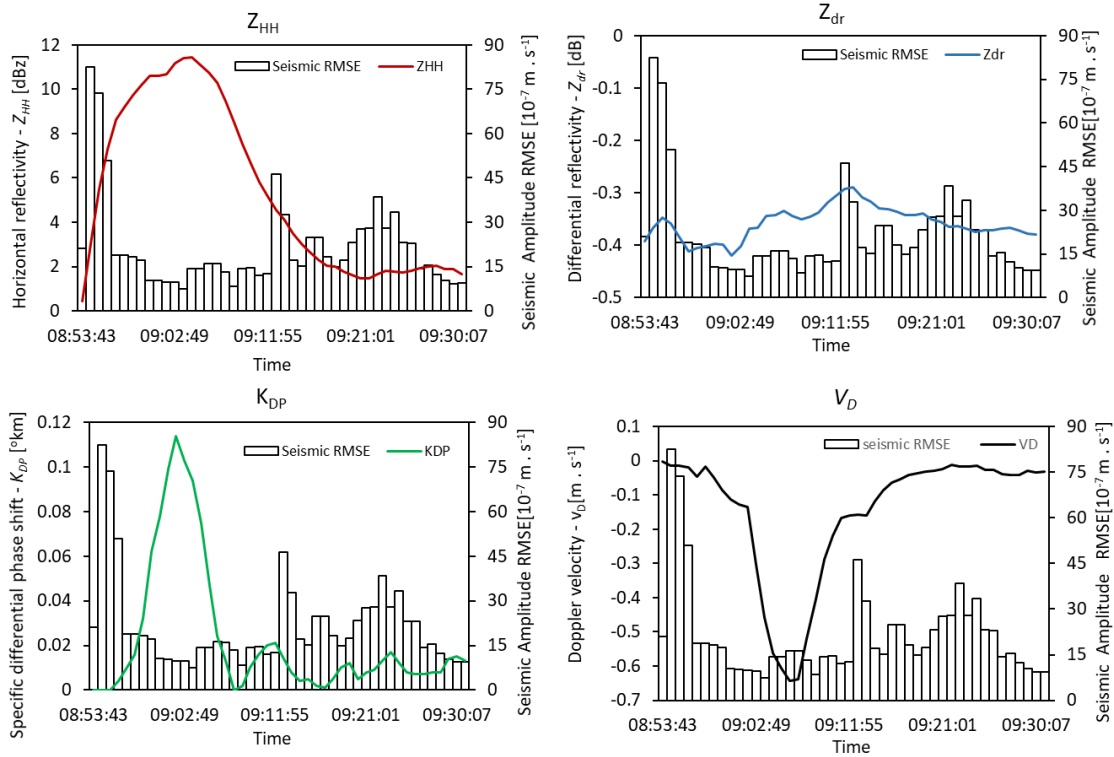Kyoto University Research Information Repository

**Fig. 4.** Temporal changes in the mean values of some radar parameters for the volcanic ash column of the Mt. Sinabung eruption on February 19, 2018 relative to the temporal changes of seismic amplitude.
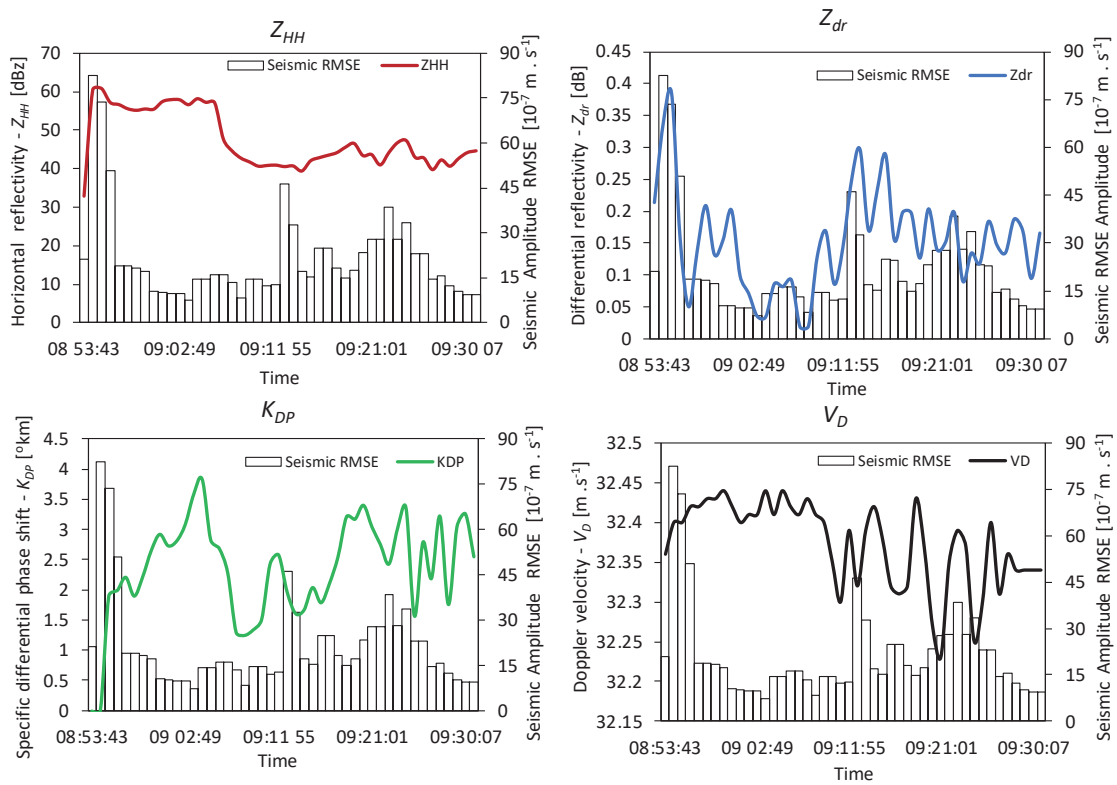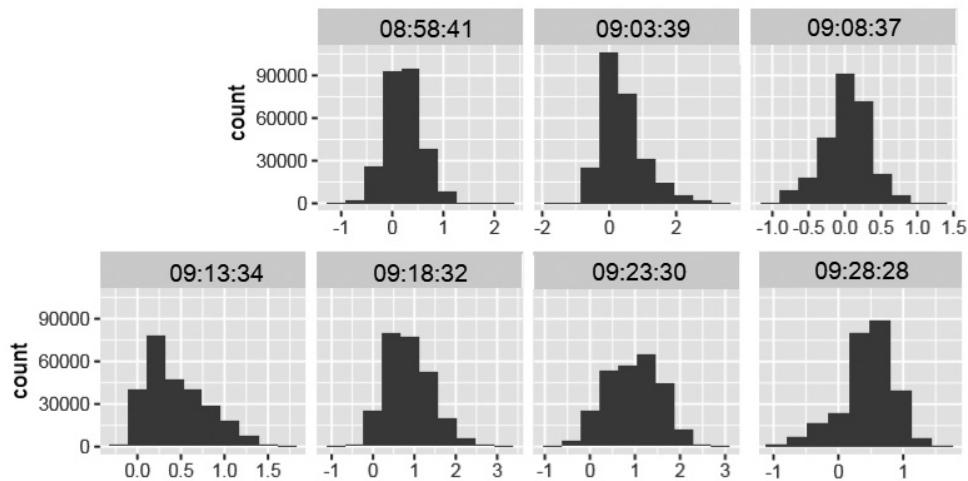


**Fig. 5.** Temporal changes in the maximum values of some radar parameters for the volcanic ash column of the Mt. Sinabung eruption on February 19, 2018 relative to the temporal changes of seismic amplitude.

**Fig. 6.** Histogram of the specific differential phase shift ($K_{DP}$). Data is from the 5 min time interval of volcanic ash cloud of Mt. Sinabung eruption on February 19, 2018.

reflectivity $Z_H$ show increasing values, similar with the changed in differential reflectivity $Z_{dr}$. On the other hand, $K_{DP}$ starts to increase 3 min after the first eruption. Both $Z_{dr}$ and $K_{DP}$ provide relative similar temporal changes with seismic amplitude (**Figs. 4** and **5**), which shows the potency of these two parameters to be involved in the volcanic ash retrieval model, similar with quantitative precipitation estimate. Differential phase shift ($K_{DP}$ [°km$^{-1}$]) is the difference between the horizontal and vertical pulses of the radar as they propagate through a medium such as rain or hail, is one of the features of X-MP radar. As it is based on the phase difference within each km, it may result in no echo or data received if the target has less than 1 km size. The other reasons of the zero $K_{DP}$ in the first three minutes after the eruption are related to the shape of ash particles and their dielectric constant.

**Figure 6** gives the data distribution of $K_{DP}$ through temporal histogram for every 5 min. Most of the scanned volcanic ash $K_{DP}$ has values below 1, but at the highest monitored $Z_H$ it has some values higher than 3. The amount of $K_{DP}$ values larger than 1 increase by the time after the eruption, which may indicate the aggregation process of volcanic ash, involves the interaction with the water vapor. However, this assumption is beyond the scope of our study and neglected in the model we adopted.

The $Z_{dr}$ indicates a comparison between polarized horizontal and vertical waves. The maximum values of $Z_{dr}$ during the eruption could reach 0.4 (**Fig. 5**), which indicated the volcanic ash might have the same shape as drizzle. However, the mean values of $Z_{dr}$ ranges fell below 0 ($-0.4$ to $-0.1$), which might indicate that most of volcanic ash particle had the same traits as the dry or wet graupel [17]. The mean $K_{DP}$ and mean $Z_{HH}$ values have the highest values, almost at the same time when the mean Doppler velocity $- V_D$ provides negative values (**Fig. 4**). This information may indicate that larger particle or higher concentration of ejected materials in the
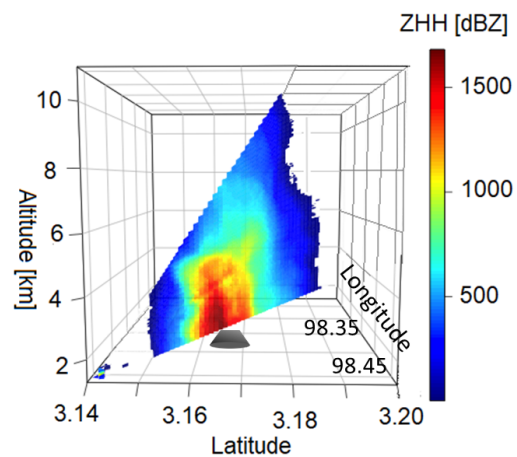


**Fig. 7.** The reflectivity factor accumulation at the 222° azimuth angle from the volcanic ash of Mt. Sinabung eruption on February 19, 2018 scanned by X-MP radar.

volcanic ash mostly moved toward the radar location.

These trends of $K_{DP}$, $Z_{HH}$, and $V_D$ in **Fig. 4** may be explained by **Fig. 7**, where the portion of the highest accumulated reflectivity factor received by the radar is distributed in the area closer to the radar site. The reflectivity factor accumulation for $\sim$37 min duration (46 scans) in **Fig. 7** also provides clearer information about the nature of volcanic eruption. The highest reflectivity factor accumulation exceeds 1500 dBZ and happens near the crater. The echo was monitored and reached more than 10.1 km altitude. The same echo distribution also gives by the spatial and temporal radar reflectivity distribution given by **Fig. 8**, where at the first 10 minutes of eruption the radar reflectivity with the highest values go to the direction toward the radar location.

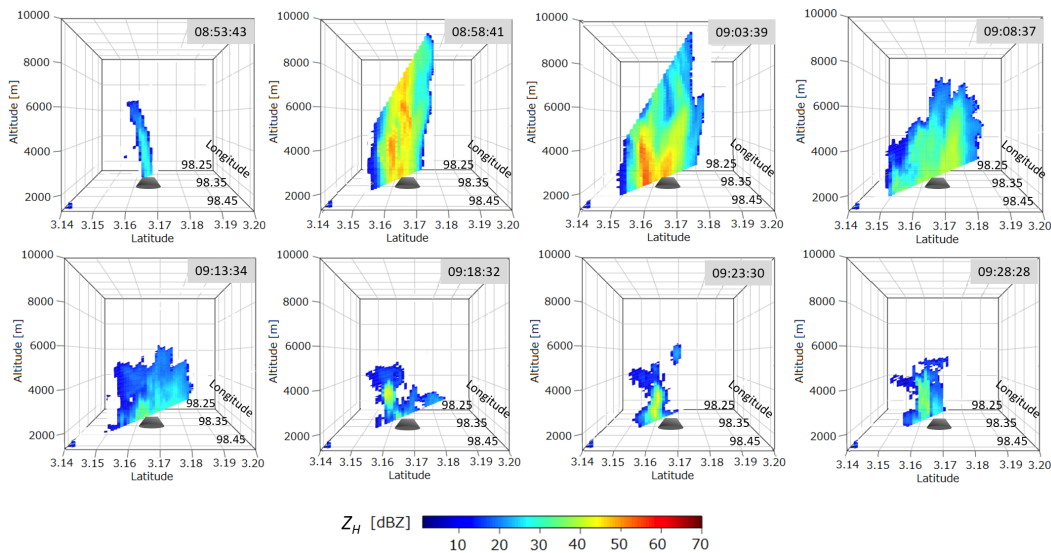Comparing with the well-developed studies on rainfall-

**Fig. 8.** The 5 min time interval of radar reflectivity $Z_H$ [dBZ] at azimuth angle 222° of the volcanic ash cloud from the Mt. Sinabung eruption on February 19, 2018. The black triangle indicates the position of Mt. Sinabung in latitude.
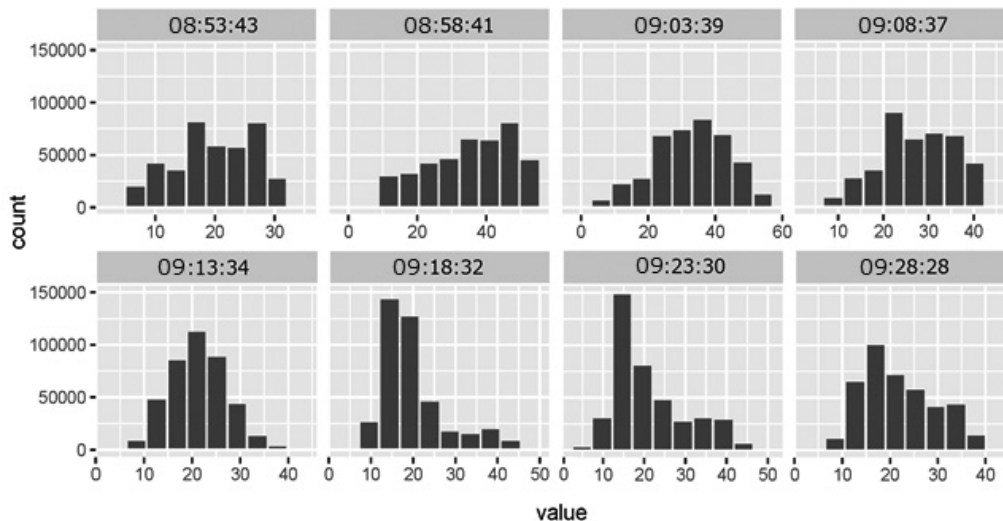


**Fig. 9.** Histogram of the radar reflectivity factor for values greater than zero. Data is from the 5 min time interval of volcanic ash cloud of Mt. Sinabung eruption on February 19, 2018.

radar algorithms, the method of volcanic ash retrieval models is mostly based on reflectivity factor and has not touched the other multi-parameters of radar. Hence, further discussion will focus on radar reflectivity factor to understand the insight on volcanic ash, in terms of retrieving the concentration and fall-rate of volcanic ash.

An increasing value of mean reflectivity factor was monitored at the early stage of the eruption (**Fig. 4**), from 0.4 dBZ (08:53:34), to be 11.4 dBZ (09:03:39). The value then decreased gradually, from 09:13:34, where the mean $Z_H = 4.1$ dBZ, to mean $Z_H = 1.7$ dBZ at 09:30:57. During the eruption from 08:54:33 to 09:30:57, the maximum echo of reflectivity monitored by radar ranges between 60.8–39.3 dBZ (**Fig. 5**). The 5-min time interval of re-

flectivity factor ($Z_{HH}$) from the SRHI scan mode of X-MP radar is given in **Fig. 8** and the histogram is shown in **Fig. 9**.

The X-MP radar could not monitor the entire volume of the ash column due to the limitations of the scan mode setting. The highest monitored altitude was approximately 7.7 km, while the diameter of the ash column seemed to be wider than the 6° of the SRHI scan. It is clear that the height of the ash column exceeds the previously reported height [2].

In the early stage of eruption, the size of volcanic ash has diameter smaller than 1 km with the maximum $Z_{HH}$ higher than 30 dBZ (**Fig. 8**). Hence this information explains the unmonitored $K_{DP}$ at the first three minutes after
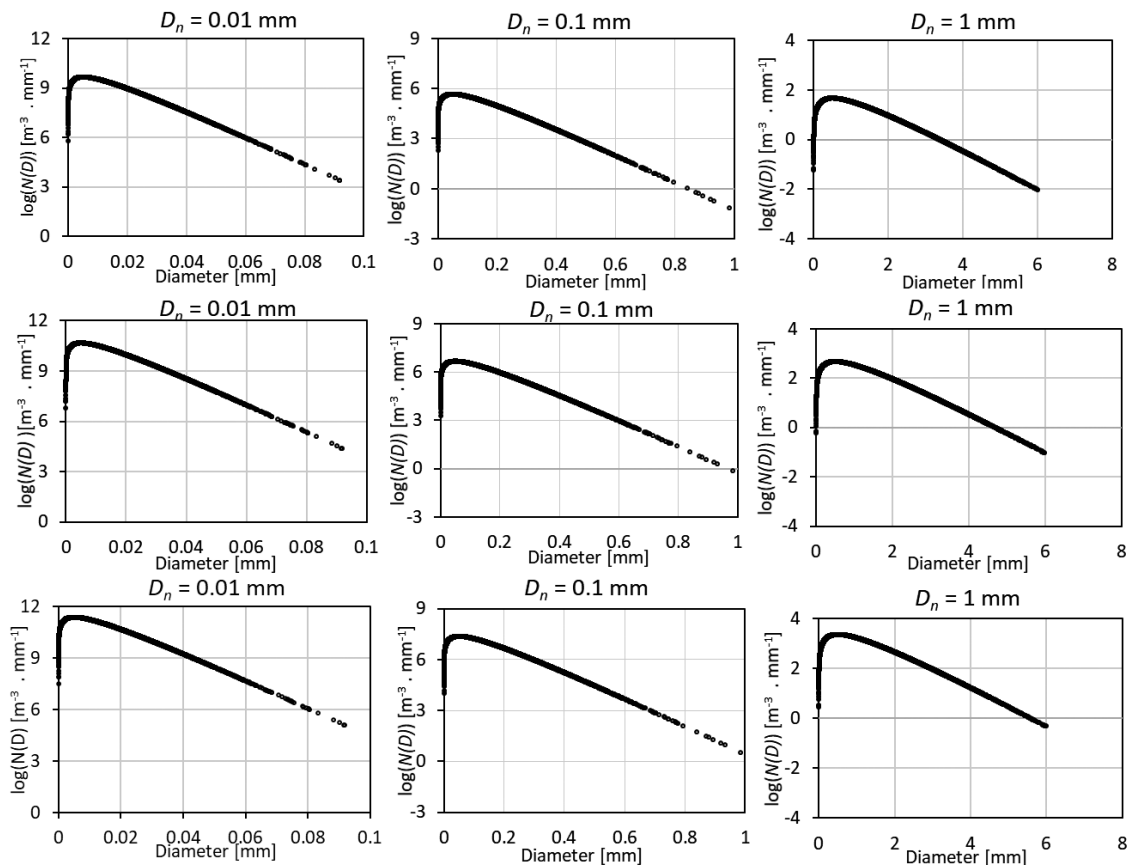
**Fig. 10.** Average PSD for the nine ash classes, divided into fine ash (left column), coarse ash (middle column), and lapilli (right column). For different concentration intensities: light (top row), moderate (middle row), and intense (bottom row), as a function of ash diameter by scaled gamma distribution.

the eruption. On the other hand, it shows to potency of X-MP radar and its fine spatial resolution (100 m mesh) to monitor the small volcanic ash column, which may not be monitored by other system such as C-band and S-band. This information is important in terms of early warning system management, as the eruption apparently started in column size smaller than 1 km.

Another report by VAAC Darwin said that the top of the volcanic ash cloud might be higher than what could be clearly observed from the ground [18]. Thus, these scan data have demonstrated the potency of X-MP radar for the precise ash column height measurement, which is important for the empirical models of emission rate.

The radar could also monitor the movement of ash particles indicated by the changes in the greater reflectivity factor during the eruption. In **Figs. 7** and **8**, greater reflectivity is concentrated in the middle of the volcanic ash column, as it may indicate coarser tephra. These larger particles are usually ejected and then dispersed after having collided with each other during the eruption. They might also fall earlier due to the gravitational force, which is indicated by the lower height of higher reflectivity factor values.

The volcanic ash was reported to be drifting to the east and south-east [18]. This report is similar to the scan image of the radar reflectivity factor in **Fig. 8**. In the early stage of eruption, a slice of RHI scan at 222° of azimuth angle presented an image of the volcanic ash column extended at 3.165–3.17°N, which was equal to 0.6 km. Five minutes later, the monitored reflectivity factor became wider at approximately 2.4 km range in the northeast to southeast (NE-SE) direction (0.022°), and at 09:03:39 it increased to 3.9 km (0.035°). The maximum diameter ash column occurred 15 min after the eruption at approximately 4.5 km NE-SE (0.04°).

The duration of the eruption was approximately 5 min so that the SRHI scanned by X-MP radar after this period, and the widening reflectivity factors, undoubtedly provided the valuable information that the pyroclastic flow happened after the eruption. This conclusion is reasonable as the same report records approximately 10 pyroclastic flow occurrences, traveling as far as 4.9 km south-southeast (SSE) and 3.5 km East [19].

### 4.2. Microphysical Parameters of Volcanic Ash

The particle size distribution (PSD) $N_a(D)$ by scaled gamma distribution of the training data are shown in **Fig. 10**. The distributions of PSD are higher in the finer particles compared to the coarser particles, which is similar to the results from the previous study [10].
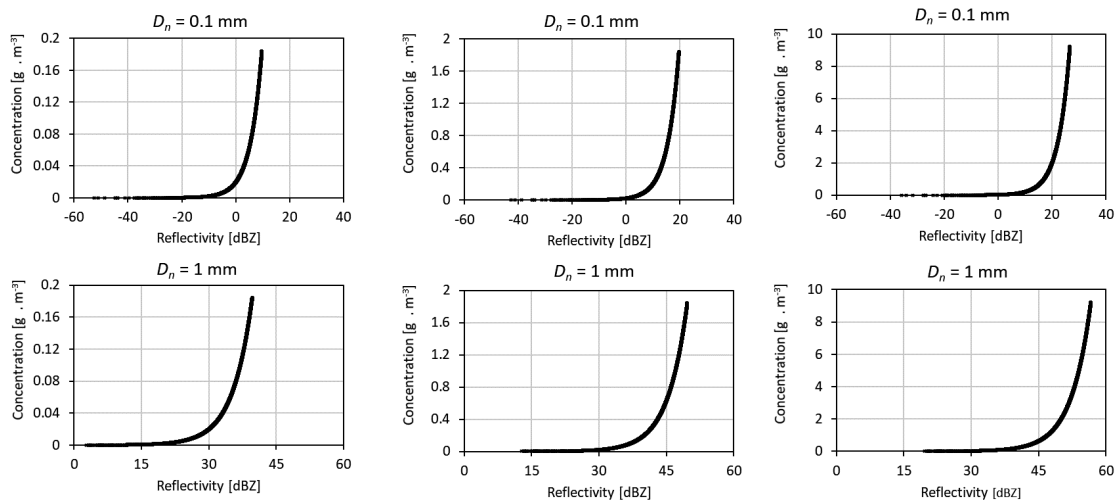
**Fig. 11.** Ash concentration as the function of reflectivity for coarse ash class (first row) and lapilli class (second row). Each class presents a different concentration intensity: light (left), moderate (center), and intense (right).



**Fig. 12.** Ash fall rate as the function of reflectivity for coarse ash class (first row) and lapilli class (second row). Each class presents a different concentration intensity: light (left), moderate (center), and intense (right).
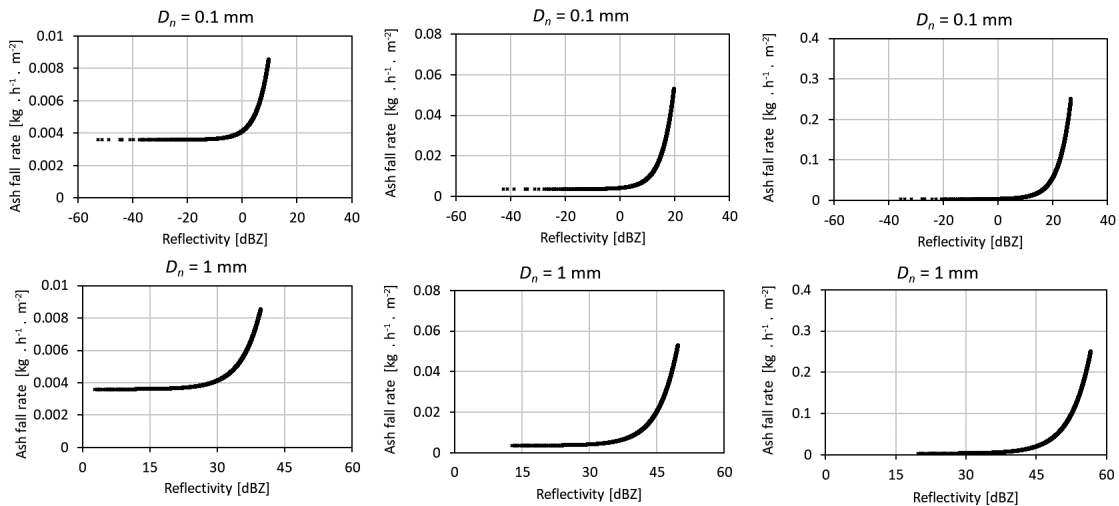
**Figures 11** and **12** present the power-law relations of ash concentration and the fall-out rate related to the reflectivity factors. The ash concentration and fall rate could increase due to either bigger particles with lower concentrations, or to the smaller ash particles with higher concentrations.

The class of fine ash for all concentration regimes had reflectivity factors lower than zero, which made them undetectable by the radar. This study used an X-MP radar at the wavelength of 3.3 cm, where the Rayleigh scattering hypothesis could be used to measure the diameter of particles up to $D \leq 2.14$ cm [20]. Although this value is much larger than the nature of volcanic ash, this is a fundamental theory that validates the use of the Rayleigh scattering theorem assumption in this case.

A previous study using the same method of ash classification [11] also found X-MP radar incapable of detecting the fine ash class at every concentration regime. Only C-band radar could estimate the fine ash class at the very intense concentrations. We can estimate the coarse ash class concentration and fall-rate if the reflectivity values are greater than zero.

### 4.3. Volcanic Ash Classification

**Table 3** presents the contingency errors for the nine ash classes based on the reflectivity factor of our training data. The total probability along a column is always equal to one, while the input classes are those listed in the columns. The error for each class classification ranges from 0 to 0.18.

The classes with moderate and intense concentrations ($C_a = 1$ g·m$^{-3}$ and 5 g·m$^{-3}$), are more difficult to predict, indicated by the probability of misclassification having a range of 0.12–0.18. However, the sum of error probability is 0.14, which is better than that in the previous classification done by Marzano et al. in 2006. That study applied

**Table 3.** Contingency error table for the nine ash size categorizations.

| Class | Fine (light) | Fine (moderate) | Fine (Intense) | Coarse (light) | Coarse (moderate) | Coarse (Intense) | Lapili (light) | Lapili (moderate) | Lapili (Intense) |
|---|---|---|---|---|---|---|---|---|---|
| **Fine (light)** | 1.00 | 0.13 | 0.04 | 0.01 | 0.00 | 0.00 | 0.00 | 0.00 | 0.00 |
| **Fine (moderate)** | 0.00 | 0.87 | 0.18 | 0.02 | 0.01 | 0.00 | 0.00 | 0.00 | 0.00 |
| **Fine (Intense)** | 0.00 | 0.00 | 0.78 | 0.06 | 0.01 | 0.00 | 0.00 | 0.00 | 0.00 |
| **Coarse (light)** | 0.00 | 0.00 | 0.00 | 0.91 | 0.12 | 0.04 | 0.01 | 0.00 | 0.00 |
| **coarse (moderate)** | 0.00 | 0.00 | 0.00 | 0.00 | 0.86 | 0.18 | 0.02 | 0.01 | 0.00 |
| **Coarse (Intense)** | 0.00 | 0.00 | 0.00 | 0.00 | 0.00 | 0.78 | 0.06 | 0.01 | 0.00 |
| **Lapili (light)** | 0.00 | 0.00 | 0.00 | 0.00 | 0.00 | 0.00 | 0.91 | 0.12 | 0.04 |
| **Lapili (moderate)** | 0.00 | 0.00 | 0.00 | 0.00 | 0.00 | 0.00 | 0.00 | 0.86 | 0.18 |
| **Lapili (Intense)** | 0.00 | 0.00 | 0.00 | 0.00 | 0.00 | 0.00 | 0.00 | 0.00 | 0.77 |

**Table 4.** Power-law equation of concentration and fall-rate as a function of reflectivity based on synthetic data.

| Class | Intensity | Power-law function |
|---|---|---|
| Coarse ash | Light | $\hat{C}_a^{(c)} = 1.04 \times 10^{-2}(Z_{Hm})^{1.23}$ |
| | | $\hat{R}_a^{(c)} = 3.07 \times 10^{-3}(Z_{Hm})^{0.42}$ |
| | Moderate | $\hat{C}_a^{(c)} = 2.44 \times 10^{-4}(Z_{Hm})^{2.97}$ |
| | | $\hat{R}_a^{(c)} = 2.04 \times 10^{-5}(Z_{Hm})^{2.61}$ |
| | Intense | $\hat{C}_a^{(c)} = 9.13 \times 10^{-6}(Z_{Hm})^{4.19}$ |
| | | $\hat{R}_a^{(c)} = 3.52 \times 10^{-7}(Z_{Hm})^{4.08}$ |
| Lapili | Light | $\hat{C}_a^{(c)} = 7.09 \times 10^{-12}(Z_{Hm})^{6.49}$ |
| | | $\hat{R}_a^{(c)} = 2.79 \times 10^{-6}(Z_{Hm})^{2.16}$ |
| | Moderate | $\hat{C}_a^{(c)} = 2.00 \times 10^{-14}(Z_{Hm})^{8.21}$ |
| | | $\hat{R}_a^{(c)} = 2.43 \times 10^{-14}(Z_{Hm})^{7.26}$ |
| | Intense | $\hat{C}_a^{(c)} = 2.57 \times 10^{-16}(Z_{Hm})^{9.42}$ |
| | | $\hat{R}_a^{(c)} = 1.79 \times 10^{-17}(Z_{Hm})^{9.19}$ |

36 sets of synthetic data to the ash classification model, derived from nine classes of ash and at four different radar distances. In their analysis, the classification error according to the naïve Bayesian classifier ranged between 0.07–0.29 [11].

Even this method cannot calculate the fine ash classes. The involvement of this class in the training is important as it is a part of the structure of the Bayesian classifier model and at the same time provides information on some volcanic ash distribution that cannot be estimated by X-MP radar.

Higher error rates in **Table 3** for higher concentration rates indicate the limitation of X-band system to give optimal estimations under this concentration regime. This is reasonable due to the Rayleigh scattering theorem used as the assumption. The previous study mentioned this limitation, where under the intense concentration regime, the lapilli class monitored by X-MP radar may not satisfy the Rayleigh scatter theorem and is better calculated by Mie scattering theorem [10].

**Table 4** explicitly lists the power-law equations for each class. Although our calculation adopted the method of Marzano et al. [10, 11], the algorithm generated in this study is different from that in the previously mentioned method. Due to different generated synthetic values, the power values of $\beta$ and $\delta$ are higher than 1, while the previous algorithm has an average value range of 0.45–0.65 [11].

The naïve Bayesian classifier is a supervised learning method as well as a statistical method of classification. It assumes an underlying probabilistic model and allows one to capture the uncertainty of a model in a principled way by determining probabilities of outcomes. This method has been widely used to solve diagnostic and predictive problems. One of the examples is its application on improving the accuracy of radar rainfall estimate by correctly identifying the systemic error [21].

Classifying the ash class before the estimation of ash parameters can have advantages on performing a stepwise regression to approximate the non-linear relation between ash parameters and radar reflectivity.

This two-step method can reduce more than 50% of the mean square error compared to a single-step approach by assuming one class of ash [11]. Using nine classes of synthetic ash data is recommended in case of lack of *in situ* data to cover a wide range of ash regimes. The given residual range of the reflectivity factor within each class might overlap, but the naïve Bayesian classifier could easily distinguish the probability density and signature of each class.

In meteorology, the classification of the hydrometeor class is important for quantitative precipitation estimates. The hydrometeor classes: graupel, snow aggregates, and ice crystals have different sizes and densities, and thus different fall velocities which contribute differently to the amount and horizontal distribution of precipitation on the ground. Applying a fuzzy cluster classification to identify the hydrometeor class was found to be consistent with the *in situ* observational data from balloon-borne instruments (hydrometeor videosondes: HYVISs) [22]. Another study has found the Bayesian classification method to be comparable or even better than the fuzzy logic based classification [23].
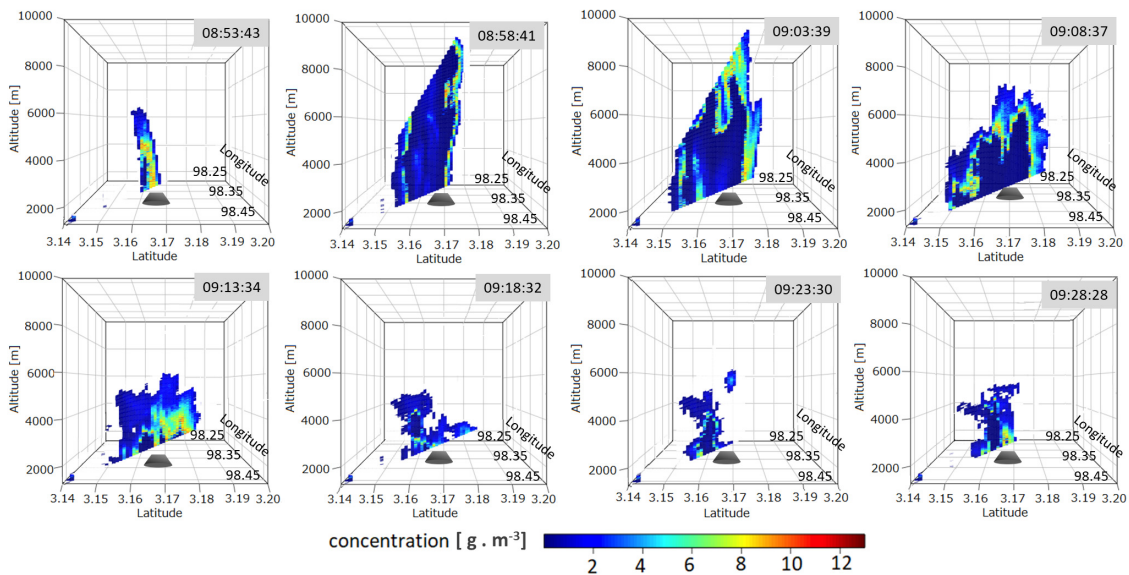
**Fig. 13.** The 5 min temporal changes of ash concentration for each bin of radar reflectivity, at the azimuth angle of 222 ∘ from Mt. Sinabung eruption on February 19, 2018. The location of Mt. Sinabung is indicated by the black triangle.



**Fig. 14.** The 5 min temporal changes of ash fall rate for each bin of radar reflectivity, at the azimuth angle of 222 ∘ from Mt. Sinabung eruption on February 19, 2018. The location of Mt. Sinabung is indicated by the black triangle.
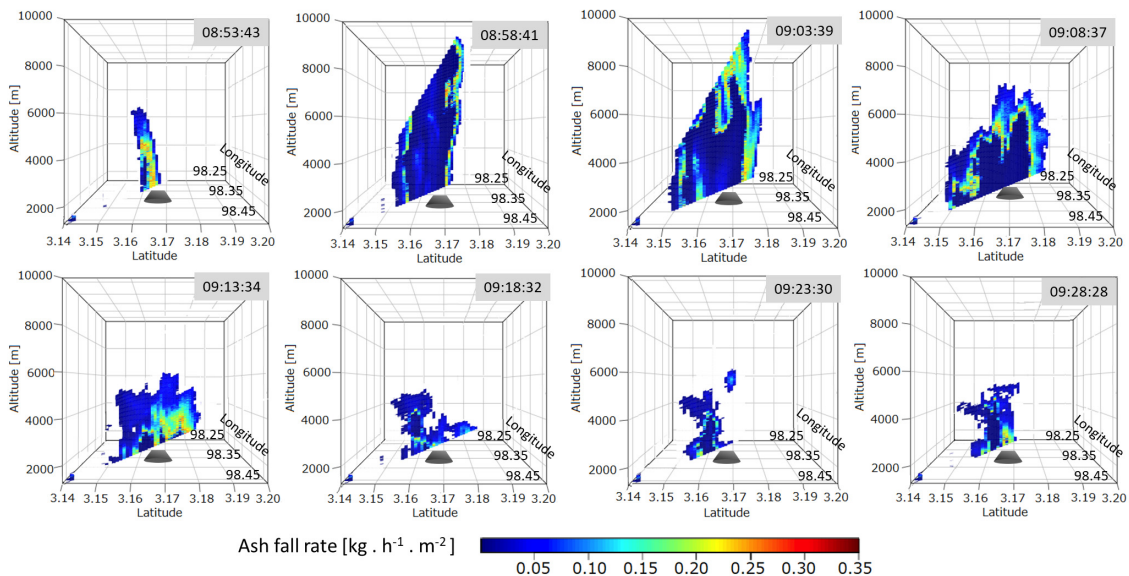
## 4.4. Ash Concentration and Fall-Out Rate Estimation

After the identification of the reflectivity factor for each class, the concentration and the fall-out rate is easily derived for each bin of the radar reflectivity factor used in the equation in **Table 4**. **Figs. 13** and **14** show the concentration at 5 min and ash fall rate from the 222° azimuth angle, respectively. Higher concentration particles were ejected at the earliest stage of eruption at 01:53:34 UTC. Maximum concentration during the eruption is 12.9 g·m$^{-3}$, and the maximum fall rate is 0.35 kg·h$^{-1}$·m$^{-2}$, which occurred in the earlier stage of erup-

tion (08:54:43). This is at about the same time as the significant increase in the RMSE of seismic amplitude (**Figs. 4** and **5**). The higher reflectivity is not always followed by higher concentration and fall rate. Thus, the regions in the inner part of the plume with higher reflectivity might be associated with the lapilli class having low concentration. These results are in agreement with the previous estimation of volcanic ash using polarimetry radar [11].

The surrounding ash plume usually consists of lower concentration and slower aggregation rate. Fine particles create greater surface area and more aggregation pro-

cesses. The process is not affected by the distance from the vent, as it may interact with water vapor. This interaction increases the cohesiveness of the ash particle when it drifts higher from the vent. This process can increase the velocity of small particles [24]. However, the interaction between water vapor and ash is disregarded in our model, as it assumes the cloud ash to be a mixture of air and dry volcanic ash.

The aggregation process of smaller particles may explain the higher concentration of the lower reflectivity, which is associated with the coarse ash class. Another reason might be due to the model assumption of the Rayleigh scatter approximation used in the model. This assumption could not estimate larger particles of ash. As for the X-band system, the Mie scattering effects might not be negligible for lapilli with large concentration, hence the Rayleigh scattering theorem may not be suitable for this ash class regime [10].

It has been mentioned previously in Section 4.1 that the reflectivity factor data holds information on both ejected volcanic ash and pyroclastic flow. At 09:13:34, the concentration and fall rate in the inner part of the volcanic ash column were higher than in the outer column (**Figs. 13** and **14**). The concentration ranged from 8 to 10 $g \cdot m^{-3}$, which were the highest values for this time scan. These results are related to the fact that the pyroclastic flow usually has higher density [25]. Thus, in the future it is important to develop a method to distinguish between the ejected materials and pyroclastic flow reflectivity factors.

The unavailability of *in situ* ground data limits the verification of our estimation. **Fig. 15** presents the total ash mass from all the 6° azimuth angles of SRHI scan mode. It is important to notice that, (1) the scan mode could not measure the entire ash plume volume in terms of its height and diameter, (2) the fine ash particles were not estimated in this model, and (3) as the volcanic ash was preserved after the eruption, the measured reflectivity factor consisted of ejected ash and pyroclastic flow. Although our data could not provide the entire estimated volcanic ash mass, considering the eruption to last approximately 5 min, we assumed the volcano ejected its materials until 7 min after the eruption (at 09:00 local time).

Thus, based on the SRHI reflectivity factors data, the model estimated the ejected materials from the eruption to be more than 0.8 million tons. The February 19, 2018 Mt. Sinabung eruption had a 2-Volcanic Explosivity Index (VEI) [19]. In general, a 2-VEI eruption can eject more than one million ton of volcanic material. Hence, our estimation is reasonable and in agreement with the known range of value.

Furthermore, as an additional comparison, we calculated the emission rate of volcanic ash using two empirical equations proposed by Mastin [26] and the VAFTAD (Volcanic Ash Forecast Transport and Dispersion) model [27]. These two empirical emission rate models provide the emission rate ($kg \cdot s^{-1}$) as a power-law function of the ash plume height (km). If we assume the plume height to be at least 9 km, values of $1.3 \times 10^6$ $kg \cdot s^{-1}$ and $1.5 \times 10^6$ $kg \cdot s^{-1}$ are estimated by Mastin's fit model and
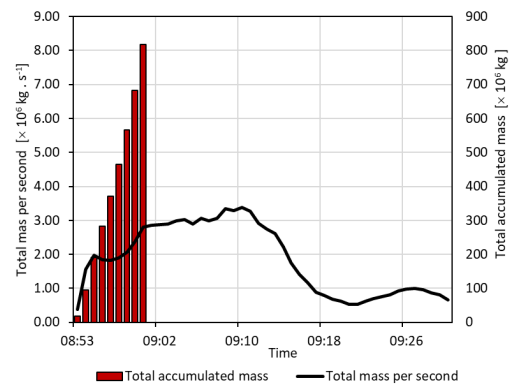


**Fig. 15.** Temporal estimated volcanic ash mass ($\times 10^6$ $kg \cdot s^{-1}$) and the total accumulation of tephra ejected from the volcano ($\times 10^6$ kg) estimated from radar reflectivity during the eruption of Mt. Sinabung on February 19, 2018.

the VAFTAD model, respectively.

These values are also comparable with our results in **Fig. 15**, where the total mass per second indicated by the black line fall in the range of $0.5$–$3.5 \times 10^6$ $kg \cdot s^{-1}$. Some of the highest values of total mass per second that happened between 09:02 to 09:14 may be assumed as a portion of volcanic ash that is still floating in the air after the eruption or transforming into pyroclastic flow.

Although there is no field verification to support and validate our results, we believe that this study is a valuable contribution to the further development of the volcanic ash remote monitoring technique using weather radar. In the future, validation of these results with field verification is required to improve the model's reliability and performance. This study used synthetic ash particles for generating the microphysical model and for its classification. Hence, future work combining measured reflectivity factor and other radar parameters, $K_{DP}$ and $Z_{dr}$, with the verified ash data might be able to minimize the misclassification of particle classes.

The future study can also include volcanic ash retrieval from different scan modes. SRHI scan mode in this study could provide only the vertical profile of the volcanic ash column, but not the spatial distribution of volcanic ash during and after the eruption. It also monitored the ash cloud in a limited range that could not represent the entire volume of the volcanic ash plume. Using plan position indicator (PPI) scan mode can provide not only the 3-D volume scan of volcanic ash column but also its spatial distribution, which improves the practical application for disaster management.

## 5. Conclusion and Future Work

Volcanic ash fall estimation using X-MP radar has been done for the Mt. Sinabung eruption on February 19, 2018. The relationships between radar reflectivity factor, ash

concentration, and ash fall rate were statistically derived by a two-steps non-linear algorithm for various ranges of ash regimes based on a scaled gamma distribution of a microphysical ash model. The two-step approximation to retrieve tephra data from radar reflectivity are the ash classification and the estimation of concentration and fall rate.

Nine sets of synthetic data on nine different classes of ash were used to train the characteristics of reflectivity factor. The results show that the higher reflectivity factors were associated with the lapilli class of lower concentration. The highest concentration mostly belonged to the coarse ash class, where the maximum value was $12.9$ g·m$^{-3}$. The same ash class gave the maximum fall rate of $0.35$ kg·h$^{-1}$·m$^{-2}$. The accumulation of volcanic ash mass ejected from the Mt. Sinabung eruption is estimated to be more than 0.8 million tons. Further works involving field verification, pyroclastic flow estimation, the algorithms of volcanic ash cloud parameters retrieval from $Z_{dr}$ and $K_{DP}$, in-depth analysis involving all radar parameters to give comprehensive information about radar data quality can improve the model performance and accuracy. An application of PPI scan mode on the other hand is considered important to provide practical aspect on volcanic ash distribution related to human life.

### Acknowledgements

**References:**

[1] M. Hendrasto, Surono, A. Budianto, Kristianto, H. Triastuty, N. Haerani, A. Basuki, Y. Suparman, S. Primulyana, O. Prambada, A. Loeqman, N. Indrastuti, A. S. Andreas, U. Rosadi, S. Adi, M. Iguchi, T. Ohkura, S. Nakada, and M. Yoshimoto, "Evaluation of volcanic activity at Sinabung Volcano, after more than 400 years of quiet," J. Disaster Res., Vol.71, No.1, pp. 37-47, 2012.

[2] AHA Center, "Mount Sinabung, Indonesia 2018 eruption and update – Flash update No.01," https://ahacentre.org/wp-content/uploads/flash-update/AHA-Flash-Update-01-Mt-Sinabung-20-Feb-2018.pdf [accessed January 21, 2019]

[3] F. S. Marzano, E. Picciotti, M. Montopolli, and G. Vulpiani, "Inside volcanic clouds – Remote sensing of ash plumes using microwave weather radars," Bull. Am. Met. Soc., Vol.94, pp. 1567-1586, 2013.

[4] A. J. Prata and C. Bernardo, "Retrieval of volcanic ash particle size, mass and optical depth from a ground-based thermal infrared camera," J. Vol.Geo. Res., Vol.186, pp. 91-107, 2009.

[5] W. I. Rose, G. J. S. Bluth, and G. G. J. Ernst, "Integrating retrievals of volcanic cloud ashcharacteristics from satellite remote sensors- A summary," Philos. Trans. R. Soc. London A, Math, Phys. Sci., Vol.358, No.1770, pp. 1585-1606, 2000.

[6] S. Wen and W. I. Rose, "Retrieval of sizes and total masses of particles in volcanic clouds using AVHRRbands 4 and 5," J. Geophys. Res. Lett., Vol.26, No.22, pp. 3389-3392, 1999.

[7] D. M. Harris and W. I. Rose, "Estimating particle sizes, concentrations, and total mass of ash in volcanic clouds using weather radar," J. Geophys. Res, Vol.88, No.C15, pp. 10969-10983, 1983.

[8] W. I. Rose, D. Delene, D. Scheneider, G. Bluth, A. Krueger, I. Sprod, C. McKee, H. Davies, and G. Ernst, "Ice in the 1994 Rabaul eruption cloud: Implications for volcano hazard and atmospheric effects," Nature, Vol.375, No.6531, pp. 477-479, 1995.

[9] M. Maki and R. J. Doviak, "Volcanic ash size distribution determined by weather radar," Proc. IGARSS, Sydney, Australia, Jul.9-13, pp. 1810-1811, 2001.

[10] F. S. Marzano, G. Vulpiani, and W. I. Rose, "Microphysical characterization of microwave radar reflectivity due to volcanic ash clouds," IEEE Trans. Geosci. Remote Sen., Vol.44, No.2, pp. 313-327, 2006.

[11] F. S. Marzano and G. Vulpiani, "Volcanic ash cloud retrieval by ground-based microwave weather radar," IEEE Trans. Geosci. Remote Sen., Vol.44, No.11, pp. 3235-3246, 2006.

[12] G. Dubosclard, R. Cordesses, P. Alard, C. Hervier, M. Coltelli, and J. Kornprobst, "First testing of a volcano Doppler radar (Voldorad) at Mt. Etna," J. Geophys. Res., Vol.26, No.22, pp. 3389-3392, 1999.

[13] P. J. Speirs and D. A. Robertson, "Measurement of airborne volcanic ash using millimeter-wave radars," 35th Conf. on Radar Meteorology, 2011.

[14] S. G. Park, V. N. Bringi, V. Chandrasekar, M. Maki, and K. Iwanami, "Correction of radar reflectivity and differential reflectivity for rain reflectivity for rain Attenuation at X band: Part I: Theoretical and Empirical Basis," J. Atmos. Ocean Tech., Vol.22, pp. 1621-1631, DOI:10.1175/JTECH1803.1, 2005.

[15] S. Oishi, M. Iida, M. Muranishi, M. Ogawa, R. I. Hapsari, and M. Iguchi, "Mechanism of volcanic tephra falling detected by X-band multi parameter radar," J. Disaster Res., Vol.11, No.1, pp. 43-52, 2016.

[16] L. Wilson, "Explosive volcanic eruptions – II: The atmospheric trajectories of pyroclasts," Geophys, J.R. Astron. Soc., Vol.30, No.2, pp. 381-392, 1972.

[17] S. Fukao and K. Hamazu, "Radar for Meteorological and Atmospheric Observation," pp. 196-200, Springer, Japan, 2014.

[18] The Watchers," Massive eruption at Sinabung volcano, ash to 16.7 km (55000 feet) a.s.l," https://watchers.news/2018/02/19/sinabung-eruption-february-19-2018/ [accessed July 28, 2018]

[19] Global Volcanism Program, "Report on Sinabung (Indonesia)," S. K. Sennert (ed.), Weekly Volcanic Activity Report, 14 February-20 February 2018, Smithsonian Institution and US Geological Survey, 2018. [accessed July 28, 2018]

[20] F. T. Ulaby, R. K. Moore, and A. K. Fung, "Microwave Remote Sensing Volume 1: Fundamentals and Radiometry," Reading, MA: Addison-Wesley, 1981.

[21] D. R. McCulloch, J. Lawry, M. A. Rico-Ramirez, and I. D. Cluckie, "Detecting bright band using AI techniques in radar hydrology," Remote Sensing for Environmental Monitoring and Change Detection (Proc. of Symp. HS3007 at IUGG2007, Perugia), IAHS publ. 316, pp. 37-46, 2007.

[22] G. Wen, A. Protat, P. T. May, W. Moran, and M. Dixon, "A Cluster-Based Method for Hydrometeor Classification Using Polarimetric Variables Part II: Classification," J. Atmos. Ocean Tech., Vol.33, pp. 45-60, DOI:10.1175/ JTECH-D-14-00084, 2016.

[23] F. Marzano, D. Scranari, M. Montopoli, and G. Vulpiani, "Supervised Classification and Estimation of Hydrometeors From C-Band Dual-Polarized Radars: A Bayesian Approach, IEEE Trans. Geosci. Remote Sen., Vol.46, No.1, 2008.

[24] G. Veitch and A. W. Woods, "Particle aggregation in volcanic eruption columns," J. Geophys. Res., Vol.106, No.B11, pp. 26425-26441, 2001.

[25] V. M. Zobin, "Seismic Signals Associated with Pyroclastic Flows, Rockfalls, and Lahars," V. M. Zobins (ed.), Introduction to Volcanic Seismology (Second Edition), Elsevier, pp. 261-293, 2012

[26] L. G. Mastin, "A multidisciplinary effort to assign realistic source parameters to models of volcanic ash-cloud transport and dispersion during eruptions," J. Volcanol. Geotherm. Res., Vol.186, pp. 10-21, 2009.

[27] J. L. Heffter and B. J. B. Stunder, "Volcanic Ash Forecast Transport and Dispersion (VAFTAD) model," Weather Forecast., Vol.8, pp. 534-541, 1993.

京都大学
KYOTO UNIVERSITY

**Name:**
Magfira Syarifuddin

**Affiliation:**
Post-doctoral Researcher, Sakurajima Volcano Research Center, Disaster Prevention Research Institute (DPRI), Kyoto University

**Address:**
1722-19 Sakurajima-Yokoyama, Kagoshima 891-1419, Japan
**Brief Career:**
2009- Lecturer, State Agriculture Polytechnic of Kupang
2018  Dr.Eng. from Graduate School of Engineering, Kobe University
2018- Post-Doctoral Researcher, DPRI, Kyoto University
**Selected Publications:**
● "Empirical Model for Remote Monitoring of Rain-Triggered Lahar in Mount Merapi," J. of Japan Society of Civil Engineers, Ser. B1 (Hydraulic Engineering), Vol.74, 2018.
● "Integrating X-MP Radar Data to Estimate Rainfall Induced Debris Flow in the Merapi Volcanic Area," Adv. Water Resources, Vol.110, pp. 249-262, 2017.
**Academic Societies & Scientific Organizations:**
● Japan Society of Hydrology and Water Resources (JSHWR)
● Japan Society of Civil Engineers (JSCE)
● Japan Geoscience Union (JpGU)
● International Society of Digital Earth (ISDE)

**Name:**
Ratih Indri Hapsari

**Affiliation:**
Associate Professor, State Polytechnic of Malang

**Address:**
Jl. Soekarno Hatta 9, Malang 65141, Indonesia
**Brief Career:**
2002- Lecturer, State Polytechnic of Malang
2011  Ph.D. from Department of Civil Engineering, University of Yamanashi
2017- Associate Professor, State Polytechnic of Malang
**Selected Publications:**
● "Ensemble Short-term Rainfall-runoff Prediction and Its Application in Urban Flood Risk Mapping," IAHS-AISH Publication, Vol.357, pp. 308-319, 2013.
**Academic Societies & Scientific Organizations:**
● International Association for Hydro-Environment Engineering and Research (IAHR)
● International Association of Hydrological Sciences (IAHS)
● Indonesian Hydraulic Engineers Association (HATHI)

**Name:**
Satoru Oishi

**Affiliation:**
Professor, Research Center for Urban Safety and Security, Kobe University

**Address:**
1-1 Rokkodai, Nada-ku, Kobe, Hyogo 657-8501, Japan
**Brief Career:**
2000 Associate Professor, University of Yamanashi
2009 Professor, Kobe University
**Selected Publications:**
● "Mechanism of Volcanic Tephra Falling Detected by X-Band Multi-Parameter Radar," J. Disaster Res., Vol.11 No.1, pp. 43-52, 2016.
**Academic Societies & Scientific Organizations:**
● Japan Society of Civil Engineers (JSCE)
● Meteorological Society of Japan (MSJ)
● American Society of Meteorology (AMS)

**Name:**
Jiro Shiokawa

**Affiliation:**
Graduate School of Engineering, Kobe University

**Address:**
1-1 Rokko-dai, Nada-ku, Kobe, Hyogo 657-8501, Japan
**Brief Career:**
2017  Graduated from Department of Civil Engineering, Kobe University
**Academic Societies & Scientific Organizations:**
● Japan Society of Hydrology and Water Resources (JSHWR)

Syarifuddin, M. et al.

**Name:**
Hanggar Ganara Mawandha

**Affiliation:**
Graduate School of Engineering, Kobe University

**Address:**
1-1 Rokko-dai, Nada-ku, Kobe, Hyogo 657-8501, Japan
**Brief Career:**
2009- Junior Engineer, Dirkse Millieutechniek B.V.
2010- Landuse Planner, Nippon Koei Co., Ltd, Indonesia
2014- Teaching Assistant, Civil and Environmental Engineering Department, University of Gadjah Mada
2018- Ph.D. Student, Graduate School of Engineering, Kobe University
2018- Lecturer, Faculty of Agricultural Technology, University of Gadjah Mada
**Academic Societies & Scientific Organizations:**
● Japan Society of Civil Engineer (JSCE)
● Indonesian Hydraulic Engineering Experts Association (HATHI)

**Name:**
Masato Iguchi

**Affiliation:**
Disaster Prevention Research Institute (DPRI), Kyoto University

**Address:**
1722-19 Sakurajima-Yokoyama, Kagoshima 891-1419, Japan
**Brief Career:**
1981- Research Associate, DPRI
1995- Associate Professor, DPRI
2012- Professor, DPRI
**Selected Publications:**
● "Contribution of monitoring data to decision making for evacuation from the 2014 and 2015 eruptions of Kuchinoerabujima Volcano," J. of Natural Disaster Science, Vol.38, pp. 31-47, 2017.
● "Volcanic activity of Sakurajima monitored using GNSS," J. Disaster Res., Vol.13, No.3, pp. 518-525, 2018.
**Academic Societies & Scientific Organizations:**
● Volcanological Society of Japan (VSJ)
● American Geophysical Union (AGU)